IEEE Access
Multidisciplinary | Rapid Review | Open Access Journal

Received December 10, 2018, accepted December 16, 2018, date of publication December 24, 2018,
date of current version January 23, 2019.

Digital Object Identifier 10.1109/ACCESS.2018.2889083

A Simple and Robust Sensorless Control Based on Stator Current Vector for PMSG Wind Power Systems

NGOC DAT DAO[1], (Student Member, IEEE), DONG-CHOON LEE[1], (Senior Member, IEEE), AND SANGMIN LEE[2]

[1]Department of Electrical Engineering, Yeungnam University, Gyeongsan 38541, South Korea
[2]Doosan Robotics, Suwon 16648, South Korea

Corresponding author: Dong-Choon Lee (dclee@yu.ac.kr)

This work was supported by the Korea Institute of Energy Technology Evaluation and Planning (KETEP) and the Ministry of Trade, Industry & Energy (MOTIE) of the Republic of Korea (No. 20173030024770).

ABSTRACT This paper proposes a novel sensorless control based on the stator current vector for permanent-magnet synchronous generators in variable-speed wind energy conversion systems. In the proposed method, the rotor angle and speed are estimated indirectly from the stator currents, where only the stator inductance is required regardless of the stator resistance. In addition, the proposed method uses one current control loop to regulate the stator current magnitude, rather than two current control loops. To eliminate the current measurement noise, the second-order generalized integrator (SOGI) with a frequency-locked loop (FLL) is utilized, which can improve the estimation performance. The proposed sensorless control method with the SOGI-FLL is simple and easy to implement while achieving a fast and accurate estimation performance of the rotor angle and speed. The feasibility of the proposed method has been verified by simulation and experimental results.

INDEX TERMS Direct drive, frequency-locked loop (FLL), permanent-magnet synchronous generator (PMSG), second-order generalized integrator (SOGI), sensorless control, wind energy conversion system (WECS).

I. INTRODUCTION

Due to the strong demand for clean and sustainable energy in the world, wind power generations have been installed at a steadily increasing rate, from offshore to even residential and urban areas [1]–[3]. Since the direct-drive multi-pole PMSGs can offer higher efficiency and reliability, simpler structure and reduced maintenance costs by eliminating gearbox, they are being employed widely for wind power systems [4]–[6]. To convert the AC output voltage of the PMSG into the DC voltage, various AC/DC converter topologies have been proposed [1], [7]. Although the use of a diode rectifier brings the advantages of low cost and simple control [8], [9], it incurs high torque ripples of the generator and increases the system power losses. On the other hand, a three-phase PWM converter is preferred to achieve high efficiency and fast dynamic performance [10], [11].

For a maximum power point tracking (MPPT) control, the speed information is indispensable. Many back-EMF-based sensorless control schemes for the PMSG have been proposed in [12] and applied widely in the field due to the simple control and good dynamic performance [13]. The back-EMF-based sensorless algorithms have been implemented in a variety of methods such as open-loop calculation [14], disturbance observer [15], [16], sliding-mode observer (SMO) [17] and other advanced methods using extended Kalman filters [18] and neural networks [19], [20]. Although the open-loop and disturbance observer methods are simple and easy to implement, their performance is affected by the inverter nonlinearities and measurement noises [12]. The SMO can improve the estimation performance with high robustness to disturbances and model uncertainties, but the chattering behavior caused by the discontinuous switch control leads to the oscillating estimation errors [21]. The second-order SMO can be a solution to eliminate the chattering, but the system complexity is increased [22]. Other advanced methods can also give high performance by mitigating the harmonic ripple in the back-EMF and parameter inaccuracy effects. However, the

structure and design of these algorithms are complicated, which need a long execution time of digital control, so that high speed microprocessors of DSPs are required. Beside the back-EMF-based model, the flux-based model is also commonly used to acquire the rotor angle information [23], [24]. In the flux model, the magnitude of rotor flux is independent of rotor speed, and the performance is also less sensitive to machine parameter uncertainties. To obtain the flux, an integration of the back-EMF is required, where many practical issues should be carefully considered, e.g., initial condition, harmonics in the inverter voltage output, noise and DC offset in the current measurements.

In general, the calculation of the back-EMF and stator flux requires the information of stator currents, terminal voltages and machine parameters. In practical applications, due to the inverter nonlinearity (e.g. dead-time, device on-drop voltages), parameter variations [25], [26] and measurement noise, the estimates of the back-EMF and stator flux are usually contaminated. As a result, the accuracy of the rotor angle and speed estimation is affected adversely. Thus, a phase-locked loop (PLL) is commonly used to extract the rotor angle from the observed back-EMF and stator flux [27], [28]. A frequency-locked loop (FLL), which is applied widely to grid synchronization [29]–[31], can also be utilized for rotor speed estimation [32]. With the FLL, the speed and angle estimations are independent of each other, whereas in the conventional phase-locked loop (PLL)-based extraction method, the speed estimation is much affected by the angle estimation.

This paper proposes a novel speed sensorless control method where the rotor angle is calculated indirectly from the angle of the stator current vector instead of back-EMF or stator flux vectors. In the proposed method, only one current controller is employed to regulate the stator current magnitude, which controls the generator torque. In addition, the proposed control does not require the stator resistance of the generator, which varies unpredictably depending on the operating temperature. Thus, the proposed method does not need an on-line resistance estimator, which is employed in some back-EMF-based methods. To enhance the estimation performance, the SOGI-FLL algorithm is utilized to filter the noise and DC-offset components in the current measurements. The rotor angle is then calculated from the filtered current signals and the rotor speed is calculated from the stator frequency which is obtained from the FLL. Finally, simulation and experiment results are shown to validate the proposed sensorless control for the PMSG of the WECS.

II. MODELING AND CONVENTIONAL CONTROL OF PMSG

A. MODELING OF PMSG

Fig. 1 shows two reference frames for modeling and control of the PMSG, including the stator $\alpha\beta$ reference frame and the synchronous dq reference frame. The α-axis is considered as the reference. The dq-axis rotates at the rotor angular velocity ω_r and the d-axis is aligned with the rotor flux vector, which coincides with the N pole of the rotor. The rotor position angle θ_r is defined as the angular displacement between the d- and α-axis.

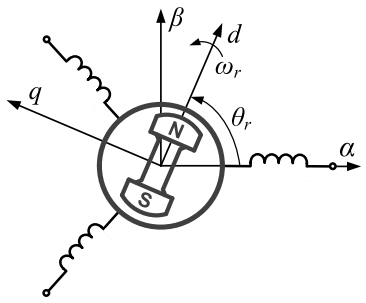

FIGURE 1. Reference frames for PMSG modeling.

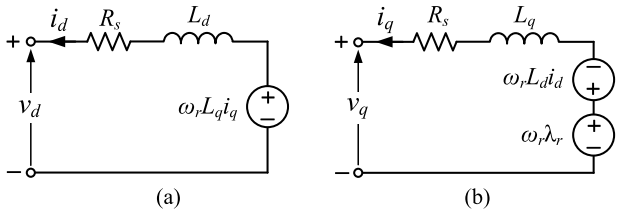

FIGURE 2. Simplified circuits of PMSG in synchronous dq frame. (a) d-axis circuit. (b) q-axis circuit.

In this study, the extended back-EMF (EEMF) modeling [16] and the extended flux modeling [23] are used since they can be applied to both the surface-mounted PMSG (SPMSG) and the interior PMSG (IPMSG). For a SPMSG, the dq-axis inductances are equal ($L_d = L_q$), but in an IPMSG, the d-axis inductance is usually lower than that of the q-axis ($L_d < L_q$).

The voltage equations of a PMSG in the synchronous dq reference frame are expressed as [16], [33]

$$\begin{bmatrix} v_d \\ v_q \end{bmatrix} = \begin{bmatrix} -R_s - pL_d & \omega_r L_q \\ -\omega_r L_d & -R_s - pL_q \end{bmatrix} \begin{bmatrix} i_d \\ i_q \end{bmatrix} + \begin{bmatrix} 0 \\ \omega_r \lambda_r \end{bmatrix} \tag{1}$$

where v_d, v_q, i_d, i_q, are the components of the stator voltages and currents in the dq reference frame, respectively, L_d and L_q are the dq-inductances, R_s is the stator resistance, p is the differential operator, and λ_r is the rotor flux produced by permanent magnets. From (1), the simplified circuits of PMSG in the synchronous dq reference frame are illustrated in Fig. 2. The electromagnetic torque of the PMSG is expressed as

$$T_e = \frac{3n_p}{2}\left[\lambda_r i_q - \left(L_d - L_q\right) i_d i_q\right] \tag{2}$$

where n_p is the number of pole pairs. In the stationary reference frame, the dynamic model of the PMSG is given as

$$\begin{bmatrix} v_\alpha \\ v_\beta \end{bmatrix} = \begin{bmatrix} -R_s - pL_d & \omega_r(L_q - L_d) \\ -\omega_r(L_q - L_d) & -R_s - pL_d \end{bmatrix} \begin{bmatrix} i_\alpha \\ i_\beta \end{bmatrix} + \begin{bmatrix} e_\alpha \\ e_\beta \end{bmatrix} \tag{3}$$

where v_α, v_β, i_α and i_β are the $\alpha\beta$-axis components of the stator voltages and currents, respectively, e_α and e_β are the

EEMF components in the $\alpha\beta$-frame, and [16]

$$\begin{bmatrix} e_\alpha \\ e_\beta \end{bmatrix} = \left[(L_q - L_d)(\omega_r i_d - \dot{i}_q) + \omega_r \lambda_r\right] \begin{bmatrix} -\sin\theta_r \\ \cos\theta_r \end{bmatrix}. \tag{4}$$

In the stationary $\alpha\beta$ reference frame, the model of PMSG can be expressed as

$$\begin{bmatrix} v_\alpha \\ v_\beta \end{bmatrix} = -R_s \begin{bmatrix} i_\alpha \\ i_\beta \end{bmatrix} + \frac{d}{dt} \begin{bmatrix} \lambda_\alpha \\ \lambda_\beta \end{bmatrix} \tag{5}$$

where λ_α and λ_β are the stator flux components in the $\alpha\beta$-axis. The relationship between the stator and rotor fluxes is given by [23]

$$\begin{bmatrix} \lambda_\alpha \\ \lambda_\beta \end{bmatrix} = \begin{bmatrix} -L_q & 0 \\ 0 & -L_q \end{bmatrix} \begin{bmatrix} i_\alpha \\ i_\beta \end{bmatrix} + \lambda_{ext} \begin{bmatrix} \cos\theta_r \\ \sin\theta_r \end{bmatrix} \tag{6}$$

where $\lambda_{ext} = \lambda_r + (L_q - L_d)i_d$ is the magnitude of the extended flux.

Based on the modeling of PMSG, there are two ways to estimate the rotor angle. In the first one, the rotor angle can be calculated directly from the EEMF in (4), as

$$\hat{\theta}_r = -\arctan(e_\alpha / e_\beta). \tag{7}$$

In the second approach, the rotor angle is calculated from the stator flux in (6), as

$$\hat{\theta}_r = \arctan\left(\frac{\lambda_\beta + L_q i_\beta}{\lambda_\alpha + L_q i_\alpha}\right). \tag{8}$$

B. FIELD-ORIENTED CONTROL OF PMSG

There are two common control methods for the PMSG, such as field-oriented control (FOC) and direct torque control (DTC) [34], [35]. In this study, the FOC is used due to its simplicity and wide acceptance for industrial drives. Fig. 3 shows a block diagram of typical sensorless FOC control for PMSGs in WECSs. The FOC is performed in the synchronous reference frame with one outer-loop speed controller and two inner-loop current controllers.

The q-axis reference current i_q^* is determined by the MPPT controller, whereas the d-axis reference current i_d^* is set to be zero or by a function of i_q^* depending on the control strategies. In practice, two control strategies are widely used for the PMSGs, such as the zero d-axis current (ZDC) control and maximum torque per ampere (MTPA) control. Usually, the SPMSG is controlled by the ZDC scheme with $i_d^* = 0$, whereas the MTPA control is applied to the IPMSG to generate the maximum torque with a minimum stator current [33].

III. PROPOSED CURRENT-BASED SENSORLESS CONTROL OF PMSG

A. ZERO D-AXIS CURRENT (ZDC) CONTROL

Normally, the multi-pole PMSGs employed in WECSs are of the surface-mounted type since it is easier to manufacture and less expensive than IPMSGs [36]. In the SPMSG, the inductances of L_d and L_q are equal [37], thus the torque equation in (2) can be simplified as

$$T_e = 1.5 n_p \lambda_r i_q. \tag{9}$$

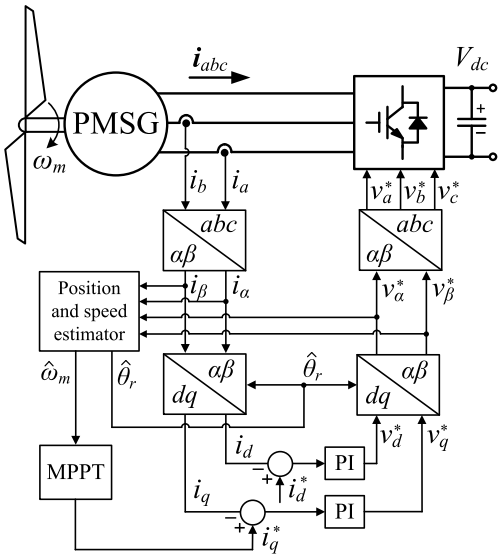

FIGURE 3. Block diagram of typical sensorless FOC control for PMSG in WECS.

Since the d-axis current does not contribute to the torque production, it is controlled at zero. Consequently, the generator torque is proportional to the stator current magnitude I_s.

In the synchronous reference frame, the d-axis is aligned with the rotor flux linkage vector $\vec{\lambda}_r$. As a result, the current vector $\vec{i}_s$ becomes perpendicular to the rotor flux vector $\vec{\lambda}_r$ when $i_d = 0$. In the steady state with ZDC control, the voltage equations in the synchronous reference frame can be simplified as

$$\begin{cases} v_d = \omega_r L_q i_q \\ v_q = -R_s i_q + \omega_r \lambda_r. \end{cases} \tag{10}$$

Fig. 4 illustrates the space vector diagram of the PMSG with the ZDC scheme. θ_r and θ_i are the angles of the rotor flux (rotor angle) and stator current vectors, respectively. It is seen in Fig. 4 that $\theta_r = \theta_i - \pi/2$.

B. PROPOSED SENSORLESS CONTROL

In the ZDC method, the angle between the stator current vector and rotor flux vector should be 90°. Based on this observation, an angle $\theta_{tr} = \theta_i - \pi/2$ is used for coordinate transformation. The angle θ_{tr} is called a transformation angle.

The block diagram of the proposed method is illustrated in Fig. 5. At the beginning, the measured stator phase currents are transformed into the stationary $\alpha\beta$ frame, as

$$\begin{bmatrix} i_\alpha \\ i_\beta \end{bmatrix} = \begin{bmatrix} 1 & 0 \\ \frac{1}{\sqrt{3}} & \frac{2}{\sqrt{3}} \end{bmatrix} \begin{bmatrix} i_a \\ i_b \end{bmatrix}. \tag{11}$$

Then, the angle of the stator current vector can be calculated by

$$\theta_i = \arctan(i_\alpha / i_\beta). \tag{12}$$

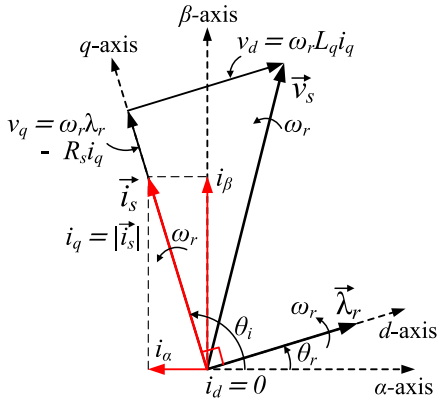

FIGURE 4. Vector diagram of PMSG with ZDC control.

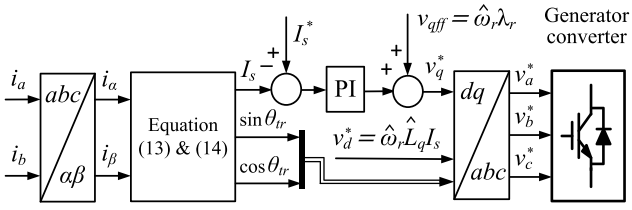

FIGURE 5. Block diagram of proposed sensorless control scheme based on stator current vector.

Since $\theta_{tr} = \theta_i - \pi/2$, the trigonometric functions of θ_{tr} can be calculated directly from the current values as

$$\sin\theta_{tr} = \frac{-i_\alpha}{\sqrt{i_\alpha^2 + i_\beta^2}}; \quad \cos\theta_{tr} = \frac{i_\beta}{\sqrt{i_\alpha^2 + i_\beta^2}}. \tag{13}$$

By using θ_{tr} to convert the stator currents from $\alpha\beta$-reference frame to dq-reference frame, the d-axis current becomes zero, whereas the q-axis current equals to the magnitude of stator currents. The d-axis current can be kept at zero without any feedback controller if the d-axis reference voltage is set to $v_d^* = \hat{\omega}_r \hat{L}_q I_s$, where $\hat{\omega}_r = d\theta_{tr}/dt$ is the estimated rotor angular velocity, $\hat{L}_q$ is the nominal value of q-axis inductance, which is measured offline before installation and I_s is the magnitude of the stator current vector, which is calculated by

$$I_s = \sqrt{i_\alpha^2 + i_\beta^2}. \tag{14}$$

In this method, the generator torque and output power are controlled by regulating I_s. The output of I_s current controller is added with a feed-forward term, $v_{qff} = \hat{\omega}_r \lambda_r$, to produce the q-axis reference voltage v_q^*. The feed-forward term v_{qff} helps to achieve a fast response to speed variations.

Using the transformation angle θ_{tr}, the voltages which are applied to the generator are obtained as

$$\begin{bmatrix} v_\alpha \\ v_\beta \end{bmatrix} = \begin{bmatrix} \cos\theta_{tr} & -\sin\theta_{tr} \\ \sin\theta_{tr} & \cos\theta_{tr} \end{bmatrix} \begin{bmatrix} v_d^* \\ v_q^* \end{bmatrix} = \begin{bmatrix} \hat{\omega}_r \hat{L}_q I_s \cos\theta_{tr} - v_q^* \sin\theta_{tr} \\ \hat{\omega}_r \hat{L}_q I_s \sin\theta_{tr} + v_q^* \cos\theta_{tr} \end{bmatrix}. \tag{15}$$

Substituting (15) into (5), the stator flux linkage components are calculated as

$$\begin{bmatrix} \lambda_\alpha \\ \lambda_\beta \end{bmatrix} = \frac{1}{\hat{\omega}_r} \begin{bmatrix} \hat{\omega}_r \hat{L}_q I_s \sin\theta_{tr} + v_q^* \cos\theta_{tr} + R_s I_s \cos\theta_{tr} \\ -\hat{\omega}_r \hat{L}_q I_s \cos\theta_{tr} + v_q^* \sin\theta_{tr} + R_s I_s \sin\theta_{tr} \end{bmatrix}. \tag{16}$$

Substituting (16) into (6),

$$\begin{bmatrix} \hat{\omega}_r \hat{L}_q I_s \sin\theta_{tr} + v_q^* \cos\theta_{tr} + R_s I_s \cos\theta_{tr} \\ -\hat{\omega}_r \hat{L}_q I_s \cos\theta_{tr} + v_q^* \sin\theta_{tr} + R_s I_s \sin\theta_{tr} \end{bmatrix} = \hat{\omega}_r \begin{bmatrix} -L_q & 0 \\ 0 & -L_q \end{bmatrix} \begin{bmatrix} i_\alpha \\ i_\beta \end{bmatrix} + \hat{\omega}_r \lambda_{ext} \begin{bmatrix} \cos\theta_r \\ \sin\theta_r \end{bmatrix}. \tag{17}$$

Then, the relationship between the transformation angle θ_{tr} and the rotor angle θ_r can be expressed as

$$\left(v_q^* + R_s I_s\right) \begin{bmatrix} \cos\theta_{tr} \\ \sin\theta_{tr} \end{bmatrix} + \hat{\omega}_r \left(L_q - \hat{L}_q\right) I_s \begin{bmatrix} -\sin\theta_{tr} \\ \cos\theta_{tr} \end{bmatrix} = \hat{\omega}_r \lambda_{ext} \begin{bmatrix} \cos\theta_r \\ \sin\theta_r \end{bmatrix}. \tag{18}$$

In (18), if the nominal q-axis inductance matches with the actual one, then the transformation angle θ_{tr} is equal to the rotor angle θ_r. Therefore, the transformation angle θ_{tr} can be used as the estimated rotor angle $\hat{\theta}_r$. As seen in (18), the variation in the stator resistance R_s does not affect the accuracy of the rotor angle estimation, whereas the variation in inductance L_q does. However, the value of L_q in SPMSGs can be regarded as constant at different operating conditions [37].

If there is a variation in the L_q, an error $\Delta\theta_r$ will appear in the estimated rotor angle. From (18), the angle estimation error can be calculated as

$$\Delta\theta_r = \arctan\left[\frac{\hat{\omega}_r (L_q - \hat{L}_q) I_s}{v_q^* + R_s I_s}\right]. \tag{19}$$

If the angle estimation error is insignificant ($\Delta\theta_r < 0.3$rad), it can be approximated as

$$\Delta\theta_r \approx \frac{\hat{\omega}_r (L_q - \hat{L}_q) I_s}{v_q^* + R_s I_s} = \frac{\hat{\omega}_r (L_q - \hat{L}_q) I_s}{\hat{\omega}_r \lambda_{ext}} = \frac{(L_q - \hat{L}_q) I_s}{\lambda_r}. \tag{20}$$

As seen in (20), the angle error is dependent not on the rotor speed, but rather on the stator current magnitude. To quantitatively evaluate the angle error caused by the inductance mismatch, a 75 kW SPMSG with parameters listed in Table 1 is investigated. Assuming the mismatch in the inductance parameter is $\Delta L = (L_q - \hat{L}_q)/L_q = \pm 20\%$, when the stator current magnitude is at the rated value of 175 A, the angle estimation error is calculated as

$$\Delta\theta_r \approx \frac{(L_q - \hat{L}_q) I_s}{\lambda_r} = \frac{\pm 20\% \times 0.00625 \times 175}{2.3} = \pm 0.095 \text{ rad} = \pm 5.45^{\circ}. \tag{21}$$

Due to the angle estimation error, an error between the produced torque and the reference one will occur, but it is

TABLE 1. Parameters of PMSG for simulation.

Parameters	Values
Rated power	75 kW
Number of poles	48
Rated voltage	380 V_{rms}
Rated speed	60 rpm
Stator resistance	0.19 Ω
dq-axis inductance	6.25 mH
Rotor flux linkage λ_r	2.3 Wb
DC-link voltage	700 V
Grid voltage	380 V / 60 Hz
Switching frequency	2.5 kHz

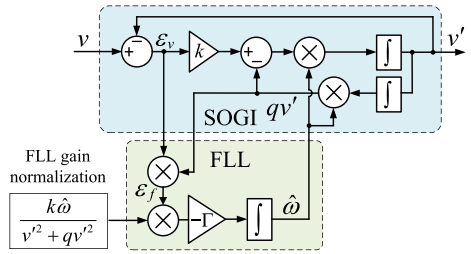

FIGURE 6. Block diagram of standard SOGI-FLL.

only 0.45%. Therefore, it can be concluded that even if the inductance value varies, the controller tracks the rotor angle with acceptable accuracy and the torque error is negligible.

IV. SOGI-FLL FOR ANGLE AND SPEED EXTRACTION

In the proposed method, the rotor angle can be calculated from the stator currents using the trigonometric functions in (13). However, the estimation performance is deteriorated by the noise in the current signals. To improve the rotor angle and speed estimation performance, the SOGI-FLL [29]–[31] is applied, which can eliminate the noise and switching harmonics in the current measurements. In addition, the FLL associated with the SOGI can estimate the fundamental frequency of the stator currents, from which the rotor speed is calculated.

A. STANDARD SOGI-FLL

Fig. 6 show the block diagram of the standard SOGI-FLL [38], from which the transfer function is given by

$$\frac{v'}{v} = \frac{k\hat{\omega}s}{s^2 + k\hat{\omega}s + \hat{\omega}^2} \tag{22}$$

where v, v' and k are the input, output signals and the gain of SOGI, respectively, and $\hat{\omega}$ is the estimated angular frequency obtained from the FLL. The transfer function in (22) represents a band-pass filter, whose bandwidth depends only on the gain k, not the frequency $\hat{\omega}$ [38].

In the FLL block, the FLL gain Γ is normalized with the amplitude of the input signal, and then the transfer function of the FLL is given by [38]

$$\frac{\hat{\omega}}{\omega} = \frac{\Gamma}{s + \Gamma} \tag{23}$$

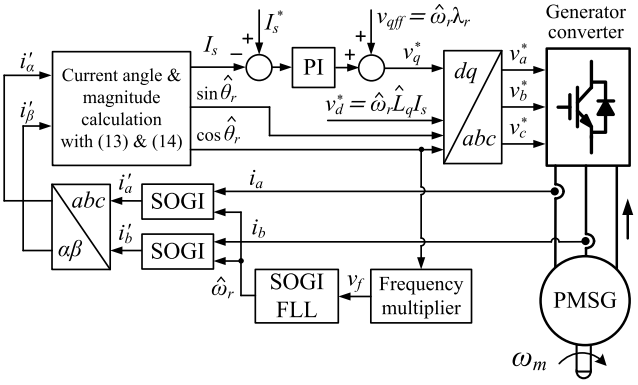

FIGURE 7. Block diagram of proposed sensorless control with SOGI-FLL.

where ω is the frequency of the input signal. From (23), the settling time of the FLL can be approximated as

$$t_{s(FLL)} \approx \frac{5}{\Gamma}. \tag{24}$$

For better tuning of the FLL, a more detailed modeling of the SOGI-FLL is considered [39], where the influence of operating frequency on the response of the FLL is taken into account. In [39], the dynamic transfer function of SOGI-FLL is obtained as

$$\frac{\hat{\omega}}{\omega} = \frac{(k\omega/2)\Gamma}{s^2 + (k\omega/2)(s + \Gamma)}, \tag{25}$$

The transfer function of the FLL has the characteristic polynomial as

$$s^2 + 2\zeta\omega_n s + \omega_n^2 = 0 \tag{26}$$

where ζ is the damping factor and ω_n is the natural frequency. As a rule of thumb, a good tradeoff between the settling time and overshoot can be achieved with $\zeta = 1/\sqrt{2}$. From (25) and (26), the FLL gain Γ can be found as

$$\Gamma = \frac{k\omega}{8\zeta^2} = \frac{k\omega}{4}. \tag{27}$$

B. APPLICATION OF SOGI-FLL TO PROPOSED METHOD

The SOGI-FLL algorithm is applied to the proposed sensorless control method, of which block diagram is shown in Fig. 7. The stator currents of the generator are measured and then filtered with the SOGI. Since the electrical frequency of the direct-drive PMSG is relatively low, the FLL gain Γ selected by (27) is a low value, at which the response of FLL will be slow. To improve the dynamic response of the FLL, an additional SOGI-FLL is utilized with a frequency multiplier, where the frequency of $\cos\hat{\theta}_r$ can be multiplied by eight as

$$\begin{aligned} v_f &= 2\left[2\{2(\cos\hat{\theta}_r)^2 - 1\}^2 - 1\right]^2 - 1 \\ &= \cos 8\hat{\theta}_r \end{aligned} \tag{28}$$

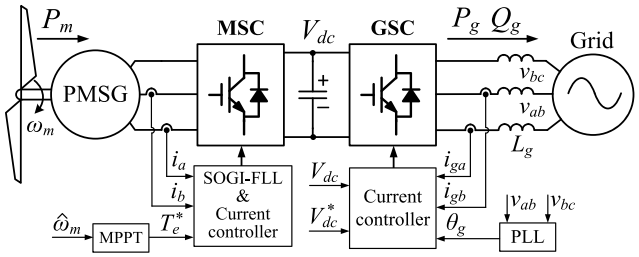

FIGURE 8. Block diagram of WECS for simulation.

where v_f is the output signal of the frequency multiplier. From (27), the Γ can be set eight times higher, then the settling time of the FLL in (24) is decreased by one eighth. In direct-drive WECS, the operating range of the PMSG whose parameters are listed in Table 1 is considered from 10 rpm to 60 rpm. By multiplying the electrical frequency at the lowest operating speed by eight in (28), then from (27), the Γ can be set at 80 with $k = \sqrt{2}$.

V. SIMULATION RESULTS

To verify the performance of the proposed method, simulation studies are conducted for a 75 kW direct-drive SPMSG WECS [40]. The configuration of the WECS is shown in Fig. 8, where the power from the wind turbine is converted and delivered to the AC grid via a full-scale back-to-back converter system. The machine-side converter (MSC) controls the generator torque to follow the optimal torque calculated from the MPPT block. The grid-side converter (GSC) is responsible for maintaining the DC-link voltage and controlling the active and reactive power transferred to the grid.

Firstly, the steady-state and dynamic performances of the proposed sensorless control method are investigated. For this test, the generator is driven not by a wind turbine, but by a prime mover. Fig. 9 shows the performance of the proposed method during the startup and subsequently the acceleration period. At the beginning, the prime mover speed is set at 10 rpm. At t = 0.1 s, the generator begins to operate for power generation and the stator current magnitude is set at 20 A. As seen in Fig. 9, after activating the controller, the estimated rotor angle $\hat{\theta}_r$ immediately follows the real one θ_r. In the meantime, the stator currents rapidly reach their steady states with the amplitude of 20 A. It takes about 100 ms for the FLL to estimate the rotor speed after the controller is activated. To show the effectiveness of the SOGI-based filters, a random noise of 10% of the stator current magnitude is added in the current measurements. For t < 0.5 s, the rotor angle is calculated directly from the measured currents. As seen in Fig. 9(e), the estimated angle is contaminated with noise for t < 0.5 s. When the SOGIs are activated for current filtering (t > 0.5 s), the noise in $\hat{\theta}_r$ is eliminated. For t > 0.8 s, the generator speed is accelerated from 10 rpm to 40 rpm at the slew rate of 300 rpm/s. Fig. 9(c) and (e) show that the stator currents are well regulated and the estimated angle

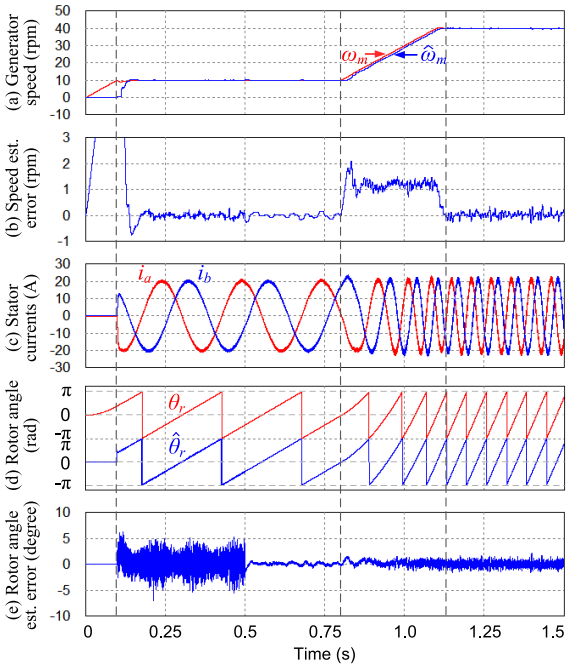

FIGURE 9. Performance of the proposed method during startup and acceleration period. (a) Generator speed. (b) Speed estimation error. (c) Stator currents. (d) Rotor angle. (e) Rotor angle estimation error.

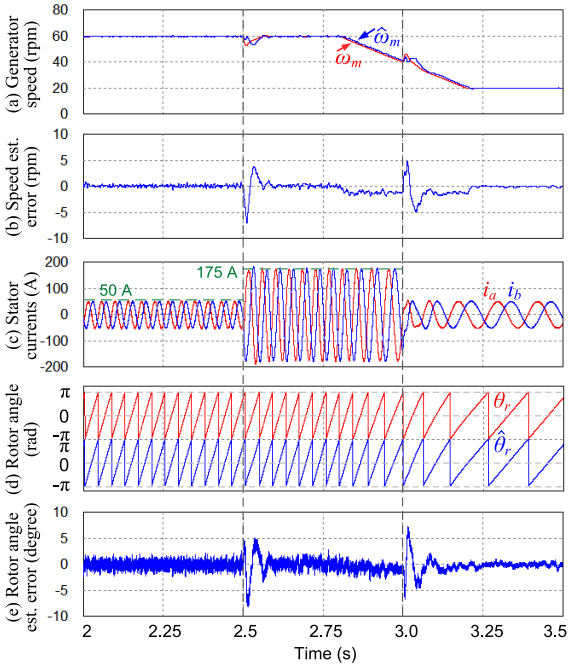

FIGURE 10. Dynamic performance of the current controller at rated speed and during deceleration period. (a) Generator speed. (b) Speed estimation error. (c) Stator currents. (d) Rotor angle. (e) Rotor angle estimation error.

follows the real one without any steady-state error even while the rotor is accelerated.

Fig. 10 shows the dynamic performance of the current controller at rated speed and subsequently during the deceleration period. Initially, the stator current magnitude is controlled at 50 A and the rotor speed is 60 rpm. At t = 2.5 s, the current

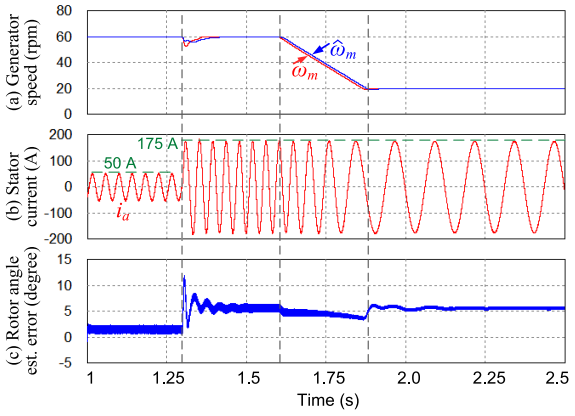

FIGURE 11. Performance of the proposed method for $\hat{L}_q = 0.8L_q$. (a) Generator speed. (b) Stator current. (c) Rotor angle estimation error.

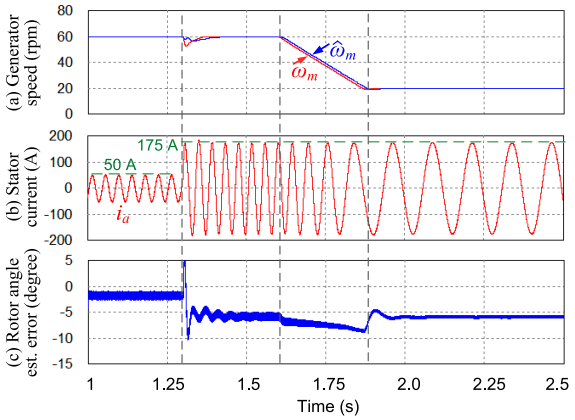

FIGURE 12. Performance of the proposed method for $\hat{L}_q = 1.2L_q$. (a) Generator speed. (b) Stator current. (c) Rotor angle estimation error.

magnitude reference is set at 175 A (rated value). At t = 2.8 s, the rotor speed is decreased from 60 rpm to 20 rpm with the slew rate of -300 rpm/s. During the deceleration period, at t = 3.0 s, the current magnitude reference is reduced to 50 A. Fig. 10(c) shows that the current controller quickly responds for the step change in the reference without any overshoots or oscillations. In transient conditions, there are disturbances in the rotor angle and speed estimations, which decay soon.

Fig. 11 and Fig. 12 show the performances of the rotor angle estimation with the inductance variation as $\Delta L = \pm 20\%$. It can be concluded from these responses that the angle estimation error is dependent on the stator current magnitude, not on the operating speed. Furthermore, when the current is 175 A, the angle error is about $\pm 5.45^{o}$, which is the same as the value computed in (21). There are variations in the angle error when the current magnitude jumps from 50 A to 175 A, but the angle error reaches quickly the steady-state value.

Fig. 13 shows the simulation results when the generator is driven by a wind turbine, where the wind speed varies randomly between 2 m/s and 10 m/s. A simple MPPT algorithm is applied [12], where the generator torque is controlled as

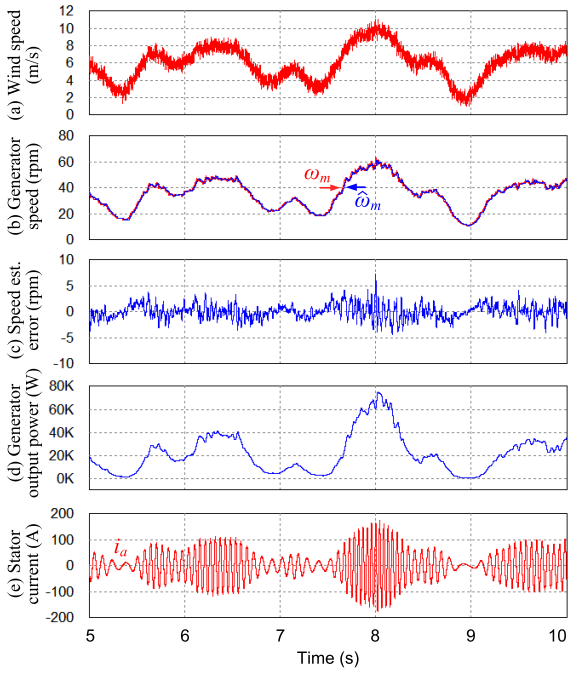

FIGURE 13. Performance of the PMSG in WECS for a variable wind speed. (a) Wind speed. (b) Generator speed. (c) Speed estimation error. (d) Generator output power. (e) Stator current.

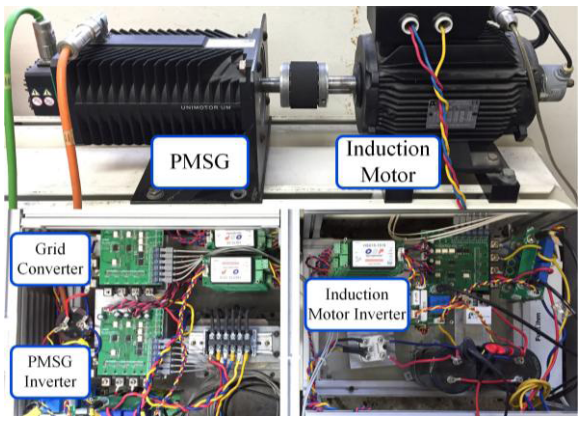

FIGURE 14. Experimental setup.

$T_e^* = K_{T,opt}\hat{\omega}_m^2$. With the proposed method, the torque is proportional to the current magnitude. Therefore, the MPPT can be achieved by controlling the current magnitude as $I_s^* = K_{I,opt}\hat{\omega}_m^2$. The coefficient $K_{I,opt}$ is constant, which is calculated from the parameters of the system. Although the wind speed varies randomly, the estimated speed can track the real one and the estimation error is kept within the range of ±5 rpm.

VI. EXPERIMENT RESULTS

A reduced-scale prototype has been built to verify the performance of the proposed sensorless control method. A photo of the experimental setup is shown in Fig. 14, where the wind turbine characteristic is simulated by the control of induction motor drive. The system parameters are listed in Table 2.

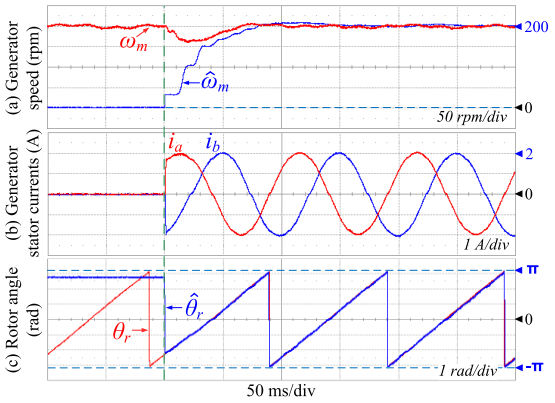

FIGURE 15. Performances of the proposed sensorless control during startup at 200 rpm. (a) Generator speed. (b) Generator currents. (c) Rotor angle.

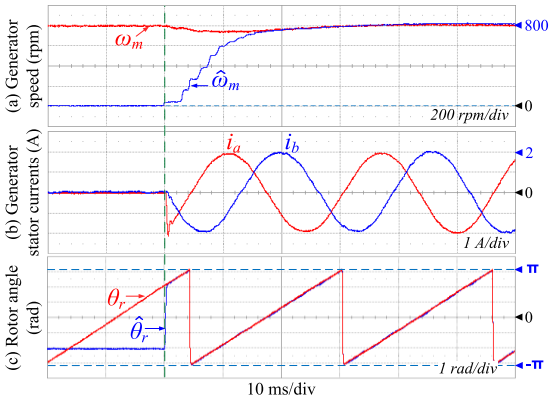

FIGURE 16. Performances of the proposed sensorless control during startup at 800 rpm. (a) Generator speed. (b) Generator currents. (c) Rotor angle.

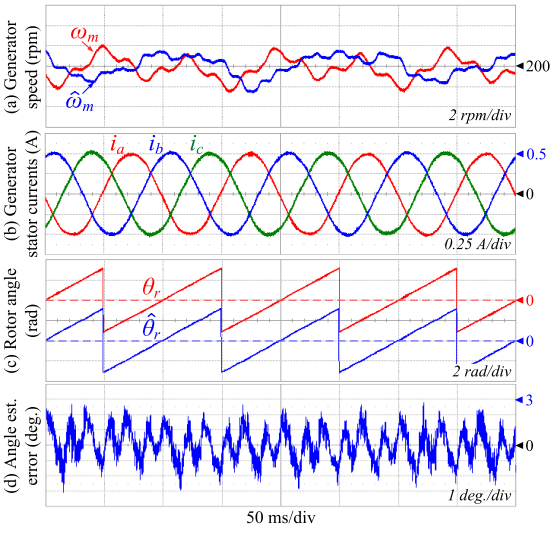

FIGURE 17. Performances of the proposed sensorless control at 200 rpm. (a) Generator speed. (b) Generator currents. (c) Rotor angle. (d) Angle estimation error.

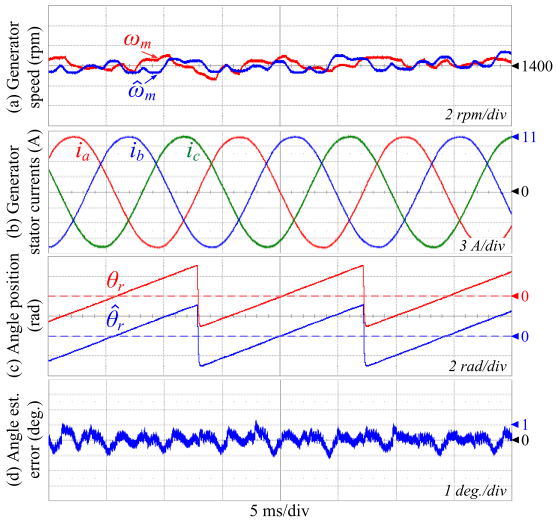

FIGURE 18. Performances of the proposed sensorless control at 1400 rpm. (a) Generator speed. (b) Generator currents. (c) Rotor angle. (d) Angle estimation error.

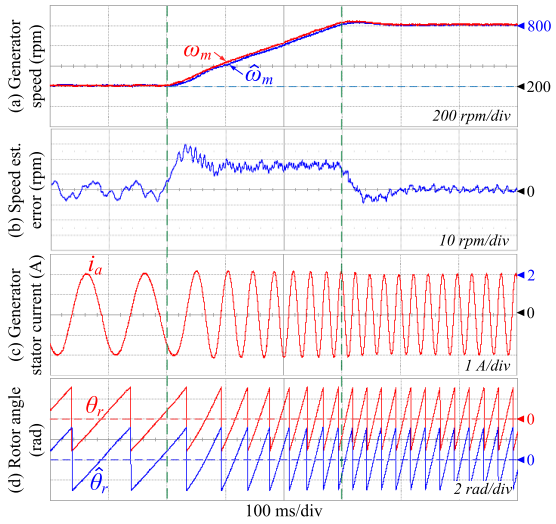

FIGURE 19. Performances of the proposed method during the acceleration from 200 rpm to 800 rpm. (a) Generator speed. (b) Speed estimation error. (c) Generator current. (d) Rotor angle.

TABLE 2. Parameters of PMSG & converter for experiment.

Parameters	Values
Rated power	2.75 kW
Number of poles	6
Rated current	8.1 A_{rms}
Torque constant	2.3 N.m/A
Stator resistance	0.49 Ω
dq-axis inductance	5.35 mH
DC-link voltage	350 V
Grid voltage	220 V / 60 Hz
Switching frequency	5 kHz

A 4096-ppr incremental encoder and hall sensors are used to monitor the actual rotor angle and speed, which are used only for comparison with the estimated angle and speed.

Fig. 15 and Fig. 16 show the performances during startup period at 200 rpm and 800 rpm, respectively. When the controller is activated, the estimated angle immediately tracks the

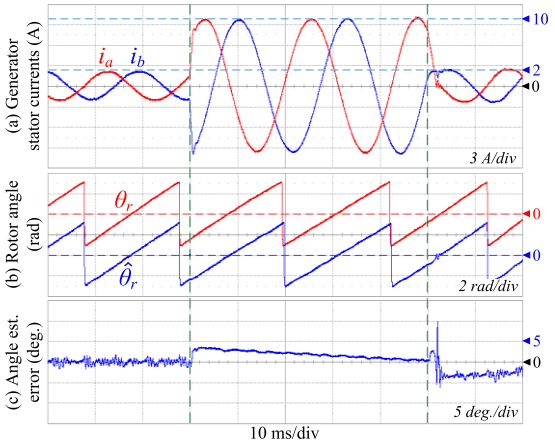

FIGURE 20. Dynamic performances of the current controller in the proposed method at 1000 rpm. (a) Generator currents. (b) Rotor angle. (c) Angle estimation error.

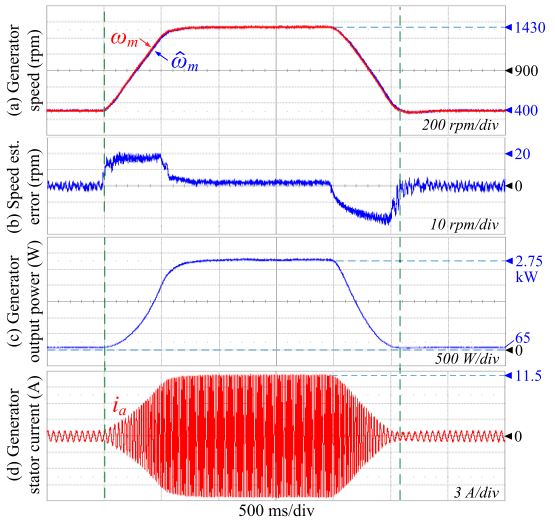

FIGURE 21. Performances of the generator with MPPT control during rapid acceleration and deceleration. (a) Generator speed. (b) Speed estimation error. (c) Generator output power. (d) Generator current.

actual one without any transient. At the same time, the stator currents quickly reach the steady-state at the reference value of 2 A. It takes about 100 ms and 20 ms for the FLL to track the actual speed at 200 rpm and 800 rpm, respectively.

Fig. 17 and Fig. 18 show the performances of the proposed control at 200 rpm and 1400 rpm, respectively. Fig. 17 shows that the controller works well even at a low value of the current reference, which is 0.5 A. At the low speed, the angle error has higher ripples due to the inverter nonlinearity, especially the dead-time effect. At 1400 rpm, the current reference is set at 11 A. The estimated speed is close to the measured one where the estimation errors are lower than 4 rpm in both the cases of Fig. 17 and Fig. 18.

Fig. 19 shows the performance when the rotor speed is increased from 200 rpm to 800 rpm at the slew rate

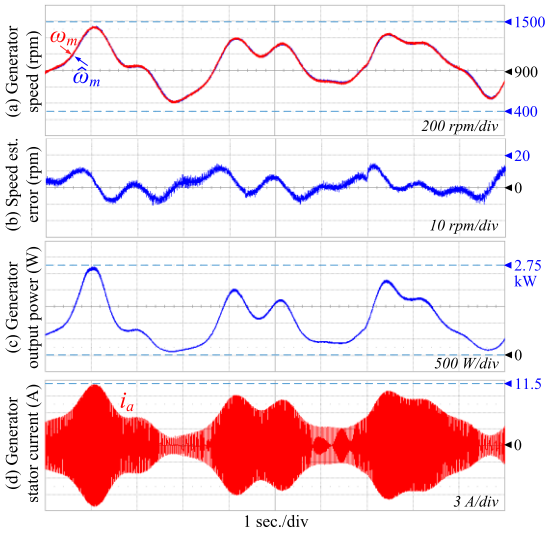

FIGURE 22. Performances of the generator with MPPT control at randomly varying speeds. (a) Generator speed. (b) Speed estimation error. (c) Generator output power. (d) Generator current.

of 2000 rpm/s. The speed estimation error is about 15 rpm/s during the acceleration period. The current is regulated closely to the reference value of 2 A. Fig. 20 shows the transient responses of the current controller for a step change of the current reference between 2 A and 10 A at 1000 rpm. Although there is an error in the estimated angle during the transient, the system remains stable and the angle error gradually decays to zero.

Fig. 21 and Fig. 22 show the system performances at variable speeds. A simple MPPT algorithm is applied, where the current is controlled as $I_s^* = K_{I,opt}\hat{\omega}_m^2$. In Fig. 21, the speed acceleration and deceleration rates are 2000 rpm/s. During these transients, there are some errors in the speed estimation, but they decay to zero when the rotor speed reaches to the steady state. In Fig. 22, the rotor speed varies at a random profile like the wind speed. The estimated speed follows well the actual one with the tracking error of $|\Delta\omega_m| < 15$rpm.

VII. CONCLUSIONS

In this paper, a simple and robust sensorless control for PMSGs in WECSs has been proposed, where the rotor angle is estimated from the stator current vector. In the proposed method, only one current control loop is used to regulate the generator torque, whereas in the conventional methods, two current control loops are required. The accuracy of the estimated angle is dependent only on the inductance parameter of the generator. The analysis for 75 kW direct-drive SPMSG WECS has shown that at rated power, if the inductance value varies as $\Delta L = \pm 20\%$, the angle error is about $\pm 5.45^o$ and the resultant torque error is only 0.45%. The proposed method can be applied to not only the SPMSG but also the IPMSG with a low saliency ratio as long as the d-axis current is controlled at zero. To improve the estimation performance,

the SOGI-FLL is utilized, which can eliminate the noise in the current measurements. The generator speed is calculated from the stator current frequency, which is extracted by the FLL. The effectiveness of the proposed sensorless method has been verified by simulation and experimental results under various conditions.

REFERENCES

[1] V. Yaramasu, B. Wu, P. C. Sen, S. Kouro, and M. Narimani, "High-power wind energy conversion systems: State-of-the-art and emerging technologies," *Proc. IEEE*, vol. 103, no. 5, pp. 740–788, May 2015.

[2] S. O. Ani, H. Polinder, and J. A. Ferreira, "Comparison of energy yield of small wind turbines in low wind speed areas," *IEEE Trans. Sustain. Energy*, vol. 4, no. 1, pp. 42–49, Jan. 2013.

[3] N. A. Orlando, M. Liserre, R. A. Mastromauro, and A. D'Aquila, "A survey of control issues in PMSG-based small wind-turbine systems," *IEEE Trans. Ind. Informat.*, vol. 9, no. 3, pp. 1211–1221, Aug. 2013.

[4] N. R. Averous *et al.*, "Development of a 4 MW full-size wind-turbine test bench," *IEEE J. Emerg. Sel. Topics Power Electron.*, vol. 5, no. 2, pp. 600–609, Jun. 2017.

[5] V. Yaramasu and B. Wu, "Predictive control of a three-level boost converter and an NPC inverter for high-power PMSG-based medium voltage wind energy conversion systems," *IEEE Trans. Power Electron.*, vol. 29, no. 10, pp. 5308–5322, Oct. 2014.

[6] S. Alepuz, A. Calle, S. Busquets-Monge, S. Kouro, and B. Wu, "Use of stored energy in PMSG rotor inertia for low-voltage ride-through in back-to-back NPC converter-based wind power systems," *IEEE Trans. Ind. Electron.*, vol. 60, no. 5, pp. 1787–1796, May 2013.

[7] Z. Chen, J. M. Guerrero, and F. Blaabjerg, "A review of the state of the art of power electronics for wind turbines," *IEEE Trans. Power Electron.*, vol. 24, no. 8, pp. 1859–1875, Aug. 2009.

[8] J. Wang, D. Xu, B. Wu, and Z. Luo "A low-cost rectifier topology for variable-speed high-power PMSG wind turbines," *IEEE Trans. Power Electron.*, vol. 26, no. 8, pp. 2192–2200, Aug. 2011.

[9] Z. M. Dalala, Z. U. Zahid, W. Yu, Y. Cho, and J.-S. Lai, "Design and analysis of an MPPT technique for small-scale wind energy conversion systems," *IEEE Trans. Energy Convers.*, vol. 28, no. 3, pp. 756–767, Sep. 2013.

[10] M. Malinowski, A. Milczarek, R. Kot, Z. Goryca, and J. T. Szuster, "Optimized energy-conversion systems for small wind turbines: Renewable energy sources in modern distributed power generation systems," *IEEE Power Electron. Mag.*, vol. 2, no. 3, pp. 16–30, Sep. 2015.

[11] A. Calle-Prado, S. Alepuz, J. Bordonau, P. Cortes, and J. Rodriguez, "Predictive control of a back-to-back NPC converter-based wind power system," *IEEE Trans. Ind. Electron.*, vol. 63, no. 7, pp. 4615–4627, Jul. 2016.

[12] Y. Zhao, C. Wei, Z. Zhang, and W. Qiao, "A review on position/speed sensorless control for permanent-magnet synchronous machine-based wind energy conversion systems," *IEEE J. Emerg. Sel. Topics Power Electron.*, vol. 1, no. 4, pp. 203–216, Dec. 2013.

[13] M. Pacas, "Sensorless drives in industrial applications," *IEEE Ind. Electron. Mag.*, vol. 5, no. 2, pp. 16–23, Jun. 2011.

[14] F. Genduso, R. Miceli, C. Rando, and G. R. Galluzzo, "Back EMF sensorless-control algorithm for high-dynamic performance PMSM," *IEEE Trans. Ind. Electron.*, vol. 57, no. 6, pp. 2092–2100, Jun. 2010.

[15] S. Morimoto, K. Kawamoto, M. Sanada, and Y. Takeda, "Sensorless control strategy for salient-pole PMSM based on extended EMF in rotating reference frame," *IEEE Trans. Ind. Appl.*, vol. 38, no. 4, pp. 1054–1061, Jul. 2002.

[16] Z. Chen, M. Tomita, S. Doki, and S. Okuma, "An extended electromotive force model for sensorless control of interior permanent-magnet synchronous motors," *IEEE Trans. Ind. Electron.*, vol. 50, no. 2, pp. 288–295, Apr. 2003.

[17] T. Bernardes, V. F. Montagner, H. A. Gründling, and H. Pinheiro, "Discrete-time sliding mode observer for sensorless vector control of permanent magnet synchronous machine," *IEEE Trans. Ind. Electron.*, vol. 61, no. 4, pp. 1679–1691, Apr. 2014.

[18] N. K. Quang, N. T. Hieu, and Q. P. Ha, "FPGA-based sensorless PMSM speed control using reduced-order extended Kalman filters," *IEEE Trans. Ind. Electron.*, vol. 61, no. 12, pp. 6574–6582, Dec. 2014.

[19] T. D. Batzel and K. Y. Lee, "An approach to sensorless operation of the permanent-magnet synchronous motor using diagonally recurrent neural networks," *IEEE Trans. Energy Convers.*, vol. 18, no. 1, pp. 100–106, Mar. 2003.

[20] X. Sun, L. Chen, H. Jiang, Z. Yang, J. Chen, and W. Zhang, "High-performance control for a bearingless permanent-magnet synchronous motor using neural network inverse scheme plus internal model controllers," *IEEE Trans. Ind. Electron.*, vol. 63, no. 6, pp. 3479–3488, Jun. 2016.

[21] H. Kim, J. Son, and J. Lee, "A high-speed sliding-mode observer for the sensorless speed control of a PMSM," *IEEE Trans. Ind. Electron.*, vol. 58, no. 9, pp. 4069–4077, Sep. 2011.

[22] D. Liang, J. Li, R. Qu, and W. Kong, "Adaptive second-order sliding-mode observer for PMSM sensorless control considering VSI nonlinearity," *IEEE Trans. Power Electron.*, vol. 33, no. 10, pp. 8994–9004, Oct. 2018.

[23] Y. Zhao, Z. Zhang, W. Qiao, and L. Wu, "An extended flux model-based rotor position estimator for sensorless control of salient-pole permanent-magnet synchronous machines," *IEEE Trans. Power Electron.*, vol. 30, no. 8, pp. 4412–4422, Aug. 2015.

[24] J. Lee, J. Hong, K. Nam, R. Ortega, L. Praly, and A. Astolfi, "Sensorless control of surface-mount permanent-magnet synchronous motors based on a nonlinear observer," *IEEE Trans. Power Electron.*, vol. 25, no. 2, pp. 290–297, Feb. 2010.

[25] K. Liu, Z. Q. Zhu, and D. A. Stone, "Parameter estimation for condition monitoring of PMSM stator winding and rotor permanent magnets," *IEEE Trans. Ind. Electron.*, vol. 60, no. 12, pp. 5902–5913, Dec. 2013.

[26] B. Nahid-Mobarakeh, F. Meibody-Tabar, and F. M. Sargos, "Mechanical sensorless control of PMSM with online estimation of stator resistance," *IEEE Trans. Ind. Appl.*, vol. 40, no. 2, pp. 457–471, Mar. 2004.

[27] X. Song, J. Fang, B. Han, and S. Zheng, "Adaptive compensation method for high-speed surface PMSM sensorless drives of EMF-based position estimation error," *IEEE Trans. Power Electron.*, vol. 31, no. 2, pp. 1438–1449, Feb. 2016.

[28] G. Zhang, G. Wang, D. Xu, and N. Zhao, "ADALINE-network-based PLL for position sensorless interior permanent magnet synchronous motor drives," *IEEE Trans. Power Electron.*, vol. 31, no. 2, pp. 1450–1460, Feb. 2016.

[29] M. Ciobotaru, R. Teodorescu, and F. Blaabjerg, "A new single-phase PLL structure based on second order generalized integrator," in *Proc. 37th IEEE Power Electron. Spec. Conf.*, Jun. 2006, pp. 1–6.

[30] P. Rodríguez, R. Teodorescu, I. Candela, A. V. Timbus, M. Liserre, and F. Blaabjerg, "New positive-sequence voltage detector for grid synchronization of power converters under faulty grid conditions," in *Proc. 37th IEEE Power Electron. Spec. Conf.*, Jun. 2006, pp. 1–7.

[31] J. S. Park, T. H. Nguyen, and D. C. Lee, "Advanced SOGI-FLL scheme based on fuzzy logic for single-phase grid-connected converters," *J. Power Electron.*, vol. 14, no. 3, pp. 598–607, 2014.

[32] N. D. Dao, D.-C. Lee, and D.-S. Lim, "Sensorless speed control of diesel-generator systems based on multiple SOGI-FLLs," in *Proc. Int. Power Electron. Conf. (IPEC-Niigata-ECCE Asia)*, May 2018, pp. 1212–1216.

[33] B. Wu, *High–Power Converters and AC Drives*, 2nd ed. Hoboken, NJ, USA: Wiley, 2017.

[34] X. Zhang, Y. He, and B. Hou, "Double vector based model predictive torque control for SPMSM drives with improved steady-state performance," *J. Power Electron.*, vol. 18, no. 5, pp. 1398–1408, 2018.

[35] X. Zhang, B. Hou, Y. He, and D. Gao, "Model predictive torque control of surface mounted permanent magnet synchronous motor drives with voltage cost functions," *J. Power Electron.*, vol. 18, no. 5, pp. 1369–1379, 2018.

[36] H. Li and Z. Chen, "Overview of different wind generator systems and their comparisons," *IET Renew. Power Generat.*, vol. 2, no. 2, pp. 123–138, 2008.

[37] S.-K. Sul, *Control of Electric Machine Drive Systems*. Hoboken, NJ, USA: Wiley, 2011.

[38] P. Rodríguez, A. Luna, R. S. Muñoz-Aguilar, I. Etxeberria-Otadui, R. Teodorescu, and F. Blaabjerg, "A stationary reference frame grid synchronization system for three-phase grid-connected power converters under adverse grid conditions," *IEEE Trans. Power Electron.*, vol. 27, no. 1, pp. 99–112, Jan. 2012.

[39] S. Golestan, J. M. Guerrero, J. C. Vasquez, A. M. Abusorrah, and Y. A. Al-Turki, "Modeling, tuning, and performance comparison of second-order-generalized-integrator-based FLLs," *IEEE Trans. Power Electron.*, vol. 33, no. 12, pp. 10229–10239, Dec. 2018.

[40] *Seoltech*. [Online]. Available: http://www.seoltech.com/eng/images/product/SWEG75K-60-I.pdf

NGOC DAT DAO (S'16) received the B.S. degree in electrical engineering from the Ho Chi Minh University of Technology, Ho Chi Minh City, Vietnam, in 2015. He is currently pursuing the Ph.D. degree with the Department of Electrical Engineering, Yeungnam University, Gyeongsan, South Korea. His current research interests include multilevel converters, high-power, high-density power converters for electric vehicles, and renewable energy systems.

DONG-CHOON LEE (S'90–M'95–SM'13) received the B.S., M.S., and Ph.D. degrees in electrical engineering from Seoul National University, Seoul, South Korea, in 1985, 1987, and 1993, respectively. He was a Research Engineer with Daewoo Heavy Industry, South Korea, from 1987 to 1988. He joined the Power Quality Laboratory, Texas A&M University, College Station, TX, USA, in 1998; the Electrical Drive Center, University of Nottingham, Nottingham, U.K., in 2001; the Wisconsin Electric Machines and Power Electronics Consortium, University of Wisconsin–Madison, WI, USA, in 2004; and the FREEDM Systems Center, North Carolina State University, Raleigh, NC, USA, from 2011 to 2012, as a Visiting Scholar. He has been a Faculty Member with the Department of Electrical Engineering, Yeungnam University, Gyeongsan, South Korea, since 1994. His current research interests include power converter design and control, renewable energy and grid connection, ac machine drives, and power quality. He served as the Editor-in-Chief for the *Journal of Power Electronics* of the Korean Institute of Power Electronics, from 2015 to 2017. He is currently the President of the Korean Institute of Power Electronics.

SANGMIN LEE received the B.S. and M.S. degrees in electrical engineering from Yeungnam University, Gyeongsan, South Korea, in 2015 and 2017, respectively. He is currently with Doosan Robotics Co., Ltd., Suwon, South Korea. His current research interests include modular dc–dc converters and machine control.